Design and multi-body dynamic analysis of the Archimede space exploration rover

Matteo Caruso *, Luigi Bregant, Paolo Gallina, Stefano Seriani

Department of Engineering and Architecture, University of Trieste, via A. Valerio 6/1, Trieste, Italy

ARTICLE INFO

MSC:
00-01
99-00

Keywords:
Planetary rover
Dynamic modeling
S-structures
Dynamic simulations
Multi-body simulations
Impact analysis
Drive analysis

ABSTRACT

In this work we present the novel planetary rover prototype "Archimede". The rover is a four wheel steering vehicle where each wheel is connected to the chassis by means of an articulated leg. These also act as a suspension system, exploiting the function of complex elastic joints named S-Structures, a series of preloaded components constituting the elastic joints. These aggregates have shown to be capable of providing compliance to otherwise stiff structures. The Kane's method is used to derive an analytical model for the dynamics of the rover, treated as a multi-body system. In the model we implement a lumped-parameters model for the S-Structure as a revolute joint with an applied non-linear torque. The soil is modeled as a rigid body and the wheel–soil interaction follows the Kelvin–Voigt model. The analytical model is validated numerically – via comparison with MSC Adams simulation software – in case of ground impact and obstacle negotiation; the experimental validation is performed on ground impact tests with a Motion Amplification high speed camera and dedicated image processing software. Results show good adherence between the models, thus validating the approach.

1. Introduction

Within the field of planetary exploration, rovers are perhaps the most flexible and enabling machines. The most recent developments have seen these robotic systems being used to manipulate equipment and sensors [1], to perform analyses on soil samples [2], and to analyze the harsh characteristics of the environment they roam [3,4]. Rovers are being designed for moving sensors [5–7], transporting soil samples [8] and manipulating small modules [9]. The Mars Sample Return (MSR) mission concept led by NASA and ESA [10] aims at delivering to Earth a sample of Mars soil to Earth in the 2030s; it is speculated that a complex architecture of rovers, landers and small martian lifters will be the means to achieve this goal [11]. In 2021, the Chinese space agency successfully deployed its rover Zhurong – part of the Tianwen-1 mission – on Mars, on the area denominated Utopia Planitia [12]. This mission is envisioned as a precursor to a sample-return mission which is planned by 2030. In these complex sample-return missions, it is required that a multitude of distinct systems are made to actively collaborate on the planetary surface, e.g. a lander with a sample-collecting rover and an ascent vehicle [13]. The current iteration for MSR by NASA-ESA envisions the Mars 2020 rover Perseverance acting as the sample-collecting rover, while a second Sample Fetch Rover (SFR) – developed by ESA – will deliver the samples to a two-stage Mars Ascent Vehicle (MAV) developed by NASA [11]. It is important to note from the same reference by Muirhead et al. that the expected traverse distance of 20 km in the allocated 150 sols would require a much higher traverse rate than those normally guaranteed by current operational Mars rovers. This aspect, together with many other related multi-agent concepts [5,9,14,15], seem to call for faster and, in general, rovers that are more capable at traversing long distances in shorter amounts of time [16]. As a brief overview of operational systems, the Perseverance rover is capable of a maximum speed of about $4.2 \times 10^{-2}\mathrm{ms}^{-1}$, the Mars Exploration Rovers Spirit and Opportunity a top speed about $5 \times 10^{-2}\,\mathrm{m\,s}^{-1}$, Curiosity has a top speed of approximately $4 \times 10^{-2}\,\mathrm{m\,s}^{-1}$ [1], Zhurong ($3.3 \times 10^{-2}\mathrm{ms}^{-1}$), Lunokhod 1 and 2 had two levels of operating speeds(approximately 0.28 and $0.56\,\mathrm{m\,s}^{-1}$). Furthermore, during space exploration missions, rovers shall be able to withstand impacts, the majority of which usually happen in the deployment phase [1]. However, when the driving speed grows, impacts can happen during obstacle and terrain negotiation [17,18]. Within this frame, we propose an in-depth study of the rover "Archimede", which is built around an innovative suspension system called S-structure (after its S-shaped elastic force–deformation plot) [17,19]. Thanks to the non-linear elastic response of this mechanism, the rover is designed to operate at high speed (1–2 $\mathrm{m\,s}^{-1}$), while at the same time allowing for shock absorption and stability of the scientific payload. Similar high-speed rover prototypes found in literature are the "Lightweight Rover

* Corresponding author.
E-mail addresses: matteo.caruso@phd.units.it (M. Caruso), bregant@units.it (L. Bregant), pgallina@units.it (P. Gallina), sseriani@units.it (S. Seriani).

Accepted 6 February 2022

Unit" (LRU) from DLR, [20] which has been designed to operate with a maximum speed of $1.1\,\mathrm{m\,s^{-1}}$; the NASA K10 rover, with a maximum speed about $1\,\mathrm{m\,s^{-1}}$; and the Dune rover [21,22] with a declared top speed of about $1.5\,\mathrm{m\,s^{-1}}$. It should be noted however, that all these rovers prototypes belong to a different class of mass with respect to the Archimede rover.

When it comes to actual planetary missions which involve the use of planetary rovers, it is important to capture every detail of the behavior of the robotic systems. The modeling of the kinematics and of the dynamics of the rover which has to be deployed is a crucial task, and one that is very much related to the success of the mission in itself. It is necessary to foresee all the different situations the rover can encounter. Kane's method allows to derive the dynamics of complex systems with ease, compared to the classical methods [23,24]. For example, Hussein et al. applied the method to the derivation of the *Equations Of Motion* (EOMs) for a three link planar arm [25]. Rambely et al. compared Kane's method with Euler–Lagrange [24]. The method was used by Pal et al. to model helicopter dynamics [26].

Lindemann showed the performance of Rover dynamics simulation with the commercial simulation software MSC Adams [27] with good results. Benamar et al. shows another implementation with the same software [28]. Chen and Genta explained how the dynamics of space exploration rovers can be described without considering the mechanics of soil by using a pseudo-coordinates model [29]; similar arguments are made by others authors as [30]. On the other hand, many authors have conducted their studies on wheel–soil interactions for soft terrains, often by modeling the soil itself via terramechanics models [31,32]. Yang et al. presented a Discrete-Element Model for lunar rovers [33] using the Bekker terramechanics theory [34]. A similar implementation is given by Ishigami et al. [35]. Schafer et al. used the simulation software SIMPACK to model rovers and soft soil [36–39].

Other research efforts explored the wheel–soil interaction in vacuum [40]; Chen et al. studied the kinematics, dynamics and trajectory control of a rover on soft terrain [41].

Based on the approach outlined by Chen and Genta [29], in this work we consider a wheel–soil interaction model described by a massless spring–damper system, which can be used in the context of contact between rigid bodies. In literature a large variety of contact models for multi-body dynamics can be found, based on the purely elastic Hertz contact theory. The most important and common models are: the Hunt and Crossley model [42] and the Lankarani and Nikravesh model [43]. In our work we implement the Kelvin–Voigt model, a visco-elastic formulation describing the contact force as a non-linear spring in parallel with a viscous linear damper [44].

In this work, we focus on the global behavior of the "Archimede" rover, rather than focusing the attention in the details of the wheel–soil interaction. Indeed, its S-Structures [18] based frame is a complex mechanism that accounts for a total of 31 *Degrees of Freedom* (DOFs) and several internal contacts that contribute to the overall dynamics in a significant way [17,19]. For this reason, as a preliminary study, a rigid multi-body system (MBS) is considered and the wheel–soil interactions are reduced to a non-linear spring damper relation with dry friction, based on the cited model [44]. We implement a lumped-element model for the leg's joints; thanks to that, we show that the Kane's method can be used to derive an analytical model for the complex dynamics of the system. Several numerical computations of this model were ran using a dedicated Runge–Kutta RK4 solver and results are compared both with a fully modeled rigid-body system simulated in MSC Adams, and with an experimental prototype. Data was acquired using high frame rate photography. Despite the many sources of inaccuracy, results show good matching between the three models, especially between the experimental and semi-analytical method. Finally, we provide an in-depth discussion on the sources of uncertainty and on the characterization of the parameters.

Finally, the contributions of this work can be summarized as follows:

- The design of a novel four wheels steering rover prototype, which uses articulated legs and complex preloaded elastic joints named S-Structures;
- Taking advantage from the S-Structures as a suspension system, together with the lightweight rover design, a rover prototype with increased driving and maneuvering speed;
- Development of a dynamics model of the rover, simplifying the complexity of the S-Structures into revolute joint with a non linear applied torque;
- Numerical validation of the rover's dynamics model through drop and drive tests and comparison with the MSC Adams multi-body simulation software;
- Experimental validation of the model through drop tests acquired with a Motion Amplification high-speed camera system on a prototype of the rover.

The present manuscript is structured as follows: in Section 2 the prototype of the four wheel steering rover is described, moreover the semi-analytical dynamics model with the Kane's method for the presented rover is derived; in Section 3 the semi-analytical model is validated through comparison with the Adams full-model of the rover and the experimental prototype. Comparison is done in the context of two different case studies and results are reported. Moreover, a sensitivity analysis on the semi-analytical model is conducted in order to characterize the influence of the uncertainty of some key parameters. In Section 4 the results are discussed, with emphasis on the characterization of the parameters and on the comparison between the three methodologies; finally in Section 5 we present the concluding remarks, which summarize the work done, and emphasize the overall merit of the effort, based on its contributions to the state of the art. Finally future works in this line of research are highlighted.

2. Model description and modeling

In this section the prototype of the Archimede four-wheel steering rover is presented and described in detail. Apart from the physical description, two distinct rover models are presented: the full rover model, and the simplified model. In the former, the full connection between the modules is implemented, while the latter a lumped-parameter approach for the S-Structures joints is adopted.

The full model is used in Adams simulations, and replicates exactly the geometry of the joints in the experimental prototype. The simplified model instead is used to simulate the rover with an ad-hoc RK4-based numerical solver. Based on the findings shown in [19], the proposed simplification is allowed.

2.1. Prototype description

The proposed rover "Archimede" is essentially based on the concept outlined by Seriani et al. in [17,19]. More precisely, it is a four wheel steering rover, in which each wheel is independent from the others and is connected to the rover chassis by means of an articulated leg (see Figs. 1(a) and 1(b)). Each leg is composed by a sequence of three modular bodies (modules), in which two contiguous modules are coupled together by a small link. Rigidity between these two contiguous modules is ensured thanks to a preloaded linear spring. This mechanism is called S-Structure and a section view can be seen in Fig. 1(c). The result is that the two bodies are coupled by means of a complex elastic connection as first described in detail in [19]. Each connection can be simplified by using a revolute joint and an equivalent preloaded torsional spring. This consideration is fundamental and will form the basis for the simplifications that will be introduced in the dynamic model

With reference to Fig. 1, the rover is designed such that the two leg bogies are connected together by means of lever mechanism. This device, which can be seen in Fig. 1(d), acts as a motion coupler between

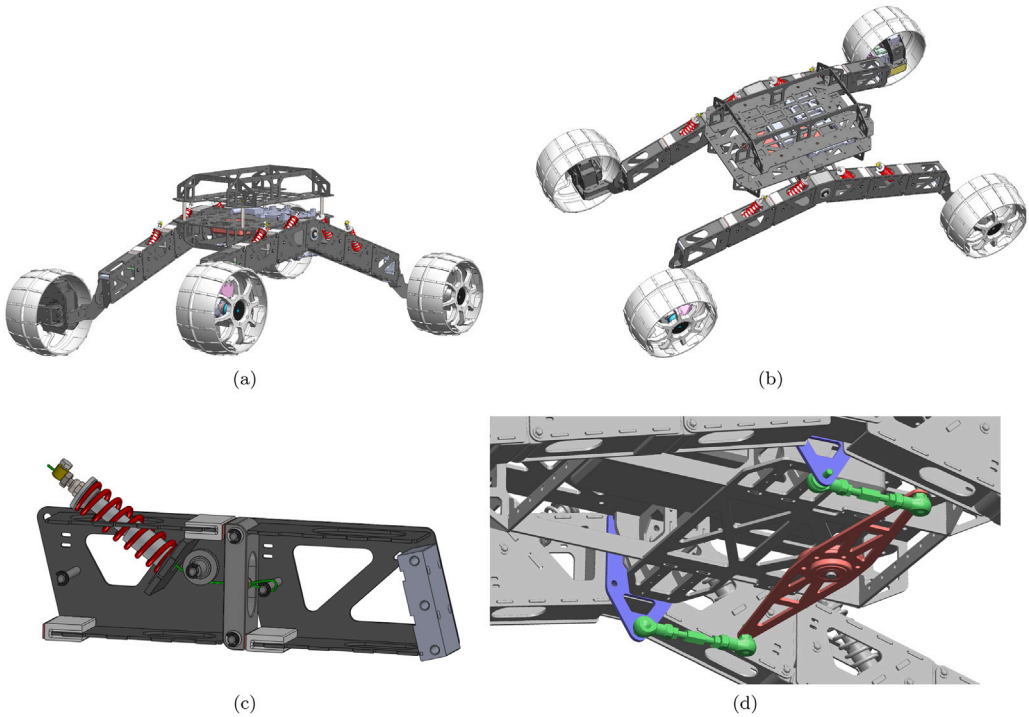

Fig. 1. In (a) and (b) different views of the CAD assembly of the Archimede rover; in (c) a section view of the single S-Structure is shown in which we see: the two contiguous modules, the connecting link, the linear preloaded spring and the redirecting pulley; finally, in (d) a view is shown of the rover, showing the lever mechanism which constrain the two bogies to rotate in opposite directions.

the bogies. More precisely, the bogies are constrained to rotate in opposite directions, thus keeping the body at an angle midway to their orientation.

With reference to Fig. 2, the wheel hub is designed such that the driving axis and the steering axis are incident and orthogonal, canceling out any offset. The wheel hub contains two independent Dynamixel XM430-350RW DC motors; one actuates the steering joint and one the wheel rotation. Although this configuration tries to simplify the wheel system, the physical dimensions of both the wheel and the articulated leg, introduce both lower and upper physical end-stops to the steering joint, which are denoted with $\delta_{j,min}$ and $\delta_{j,max}$ in Fig. 2 for a generic leg j.

Fig. 3, instead, shows each previously described element placed in the real Archimede prototype, with emphasis on design and fabrication choices. The *chassis* of the rover is made of carbon fiber composite (CFC) sheets either glued or fastened together. The single leg module, visible from Fig. 3(b), is composed by four CFC plates which constitute the housing for the preloaded spring and the deviation pulley. The connecting link between two consecutive modules is fabricated in 3D printed Polylactic Acid (PLA) polymer. The revolute joints between the modules and the connecting links are made of steel shafts supported by polymeric low-friction bearings. Each leg is then connected to the main rover body through a revolute joint visible from Fig. 3 (c–d), constituted of a steel shaft (fixed to the rover chassis) supported by ball bearings. The lever mechanism beneath the body of the rover, visible from Fig. 3(f), is made up by a large CFC arm hinged in the center to the rover belly; this is then connected to each leg by means of a steel connecting element and two spherical joints placed at its extremities. Other parts such as the wheels and the wheel hubs (Fig. 3(a)) are also fabricated in PLA through 3D printing. Finally, the rover main body, as can be seen from Fig. 3 (g–h), is made up of three different levels, each of them kept apart with steel spacers. The first layer contains the "power and electronic heart", e.g. the battery pack, the *Single Board Computer* (SBC), a Robotis OpenCR ARM Cortex-M7 based control board and the power distribution system (PDS); furthermore, the PDS and OpenCR originate the wiring which then spreads to each single

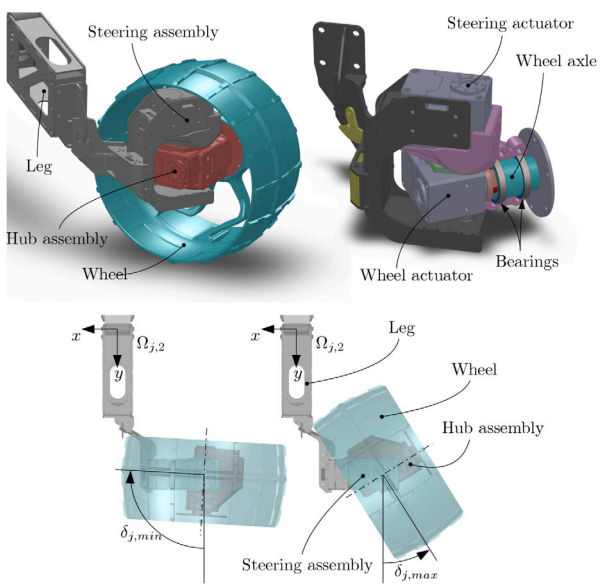

Fig. 2. Mosaic showing the wheel assembly: in the top the main components of the wheel hub are shown; in the bottom the steer angle joint limits $\delta_{j,min}$ and $\delta_{j,max}$ are indicated.

leg powering the two motors housed inside each wheel; the second level is dedicated to housing a two-dimensional Robotis LDS-01 lidar scanner; the top level instead is dedicated to a small Intel RealSense stereo-camera.

Software and control. The "brain" of the Archimede rover is a Lattepanda SBC, with Ubuntu 18.04 as the operating system; this performs most high-level functions. Mid-level control is implemented via OpenCR board, connected to the SBC via serial interface; its main function is to communicate with the individual motors. The rover

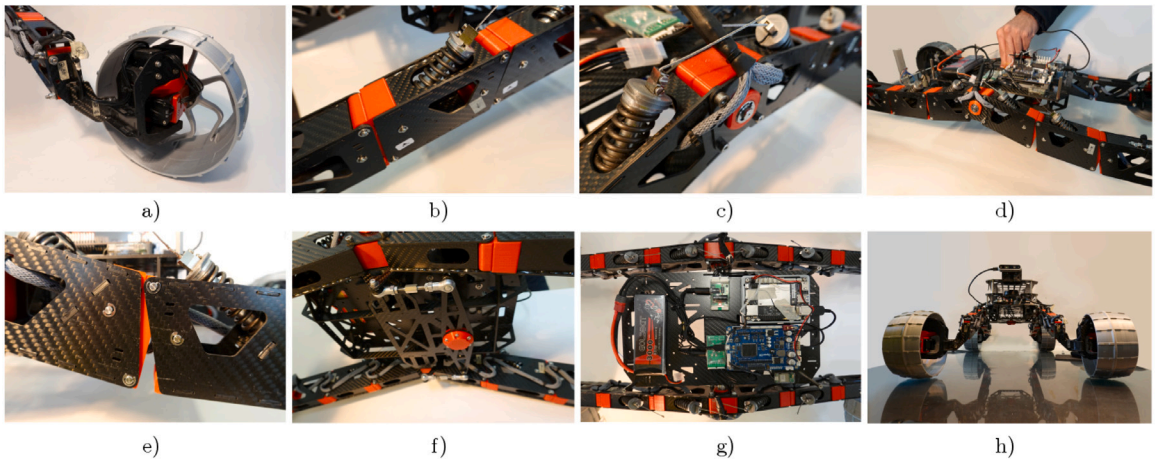

Fig. 3. In (a) a three quarter view of a wheel hub; in (b) view of the single module of the leg; in (c) view of the revolute joint connecting the leg to the rover chassis; in (d) the movement of the articulated legs under an applied vertical load; in (e) particular view of the movement of two contiguous modules, in which the small connecting link can be glimpsed, under the action of a vertical load; in (f) the view from the bottom of the lever mechanism; in (g) a view from the top of the electrical and electronic components and wiring; in (h) a view from the front showing the assembled rover.

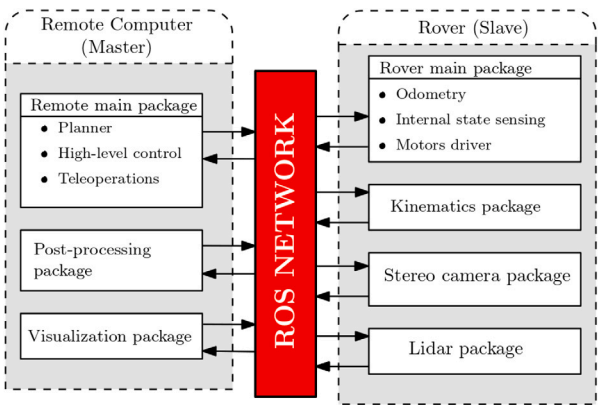

Fig. 4. Schematics of the rover's software architecture.

exploits the ROS framework, with *ad-hoc* packages developed in Python and C++. The rover prototype operates in a ROS network where the rover is the slave, while the remote computer is the master. This architecture allows only the essential elements to run in the SBC, while the heavy computational load is performed on a remote computer. The packages for the master are: the main package, which implements planning, high level control, teleoperations; the visualization package; the post-processing package. In the slave, we find the following: the main package which provides the core functionalities of the rover such as motors driver, positioning through odometry, internal state sensing; the kinematics package, which expects high level control variables from the master, computes the inverse kinematics and provides states commands for the wheel actuators. Other minor packages deployed on the SBC handle the sensors, such as the Lidar and stereo camera. The architecture is illustrated in Fig. 4.

As mentioned, the kinematics package of the robot allows for the high level control variables to be decomposed into wheel states (rotational speed for the driving wheels and angular position for the steer motors) and subsequently communicated to the motor driver, which finally applies the commands received to the single motors, through serial communication. Moreover, the kinematics package enable the rover to operate in several different driving modes: car-like steering, symmetric Ackermann steering, parallel drive, lateral drive, pure in-place rotation, general Ackermann steering etc. The same functionality takes care of handling the lower and upper joints limits of the wheel-hub.

In the following sections we describe the simplified model, together with the detailed modeling of the wheel–ground interaction and the definition of the terrain shape. The full model instead, will be described in a later section.

2.2. Analytical model

The simplified analytical dynamics model of the rover is obtained relying on three majors assumptions:

- The bodies composing the rover are treated as perfectly rigid bodies;
- The revolute joints are ideal, i.e. no joint deformation nor joint dissipative forces.
- The complex S-Structure joint is simplified with a lumped-parameters model constituted by a revolute joint with an appropriate non-linear torsional spring.

Let us introduce an inertial frame $(\mathbf{O}, \bar{\mathbf{e}}_O)$ fixed in the three dimensional Cartesian space with origin $\mathbf{O}$ and where $\bar{\mathbf{e}}_O = \{\hat{\mathbf{e}}_{O_x}, \hat{\mathbf{e}}_{O_y}, \hat{\mathbf{e}}_{O_z}\}$ is the basis vectors. Then, we introduce another reference frame $(\mathbf{G}, \bar{\mathbf{e}}_G)$ which is integral to the body of the rover and located in its center of mass $\mathbf{G}$. The rotational relation between the two frames, follows the RPY (Roll-Pitch-Yaw) convention.

The frame $(\mathbf{B}_r, \bar{\mathbf{e}}_{B_r})$, integral with the right bogie of the rover rotates about the x axis of the rover frame by an angle ϕ. The left swing arm, instead, is not independent, but it is related with the right one by a coupling relation, i.e. it rotates by the same quantity but in opposite direction, and its frame is denoted with $(\mathbf{B}_l, \bar{\mathbf{e}}_{B_l})$.

Moreover, with reference to Fig. 5, for each jth leg, with $j = 1 \dots 4$, frame $(\mathbf{\Omega}_{j,i}, \bar{\mathbf{e}}_{\Omega_{j,i}})$ is assigned to the ith module composing the leg of the rover. The frame of the ith module of the jth leg rotates about the x-axis of the upstream defined frame by an angle $\beta_{j,i}$. With reference to Fig. 5(b), the wheel-hub of the jth leg is defined by its integral frame $(\mathbf{\Gamma}_j, \bar{\mathbf{e}}_{\Gamma_j})$. The general characteristics of the wheeled system are indicated with the letters L and W for the wheelbase and the track dimensions respectively. The angles δ_j and ζ_j describe respectively the jth steering and rolling angles. The described simplified model of the rover in the three dimensional Cartesian space has 23 DOFs. By denoting with $\boldsymbol{q}$ the vector of the generalized coordinates of the system, it follows that $\boldsymbol{q} = [x, y, z, \theta, \chi, \psi, \phi, \{\beta_{j,i}\}, \{\delta_j\}, \{\zeta_j\}]$, where x, y, z are the components of the rover position vector $\boldsymbol{p}_r$ of the rover center mass in the Cartesian space relative to the inertial frame; $[\theta, \chi, \psi]$ are respectively the yaw, pitch and roll angles of the rover, $\{\beta_{j,i}\}$ is the vector of the relative rotation between the modules; $\{\delta_j\}$ and $\{\zeta_j\}$

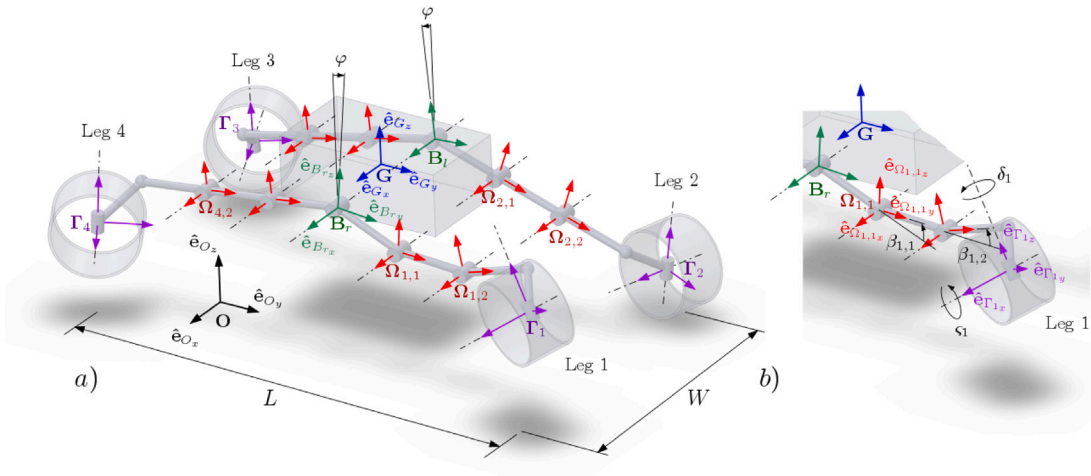

Fig. 5. In (a) the schematic representation of the simplified model of the rover is shown, with special care on indicating the involved reference frames; in (b) an expanded view can be seen of the first leg, showing its generalized coordinates.

are respectively the vectors of the steer and advance angles; where $i = 1, \dots, 2$; and $j = 1, \dots, 4$.

All the bodies composing the MBS of the rover are modeled with lumped parameters. The rover body is modeled as a box and it is characterized by having mass m_R and a full inertia tensor $\boldsymbol{I_R}$. The geometrical properties describing the bogies are the arm inclination Δ, the length of the arm l_{SA}, the offset along the x-axis of the rover frame d_{SA}. Moreover, they present physical properties of mass m_{SA} and a full inertia tensor $\boldsymbol{I_{SA}}$.

For sake of generality and coherently with the real prototype and the full rover model, the geometrical and physical parameters vary among the modules of the same leg. With reference to Fig. 5(b), consider the generic jth leg: its generic ith module is defined by having length $l_{j,i}$, mass $m_{j,i}$, a full inertia tensor $\boldsymbol{I}_{j,i}$. Its center of gravity $\mathbf{G}_{j,i}$ in general does not coincide with the module's geometric center. Finally, the wheels center of mass is characterized by having three offsets from the terminal leg module frame: the offset along the x-axis d_{j,w_x}, the one along the y-axis d_{j,w_y} and the one along the z-axis d_{j,w_z}. The physical properties of the wheels are its mass $m_{j,w}$ and in its full inertia tensor $\boldsymbol{I}_{j,w}$. However, for symmetry reasons and for global structure stability the corresponding elements have the same geometric and physical parameters even if they belong to different legs.

The described simplified model of the Archimede rover has been implemented in python, where, using Kane's method, the kinematics and the dynamic models are derived in exact form.

As stated above, the rigidity between two generic modules i and $i+1$ is ensured by a preloaded non-linear torsional spring, acting on the revolute joint $\tau_{j,i}$, for each leg j. Since the response of the preloaded spring acting between the two bodies, is a discontinuous function about the zero, its response can be described by a continuous and always differentiable approximated function [19] as follows,

$$\boldsymbol{M}_{k,\tau_{j,i}} = -\left(\frac{2M_{0,\tau_{j,i}}}{\pi}\right)\arctan\left(f\beta_{\tau_{j,i}}\right) - k\beta_{\tau_{j,i}}, \tag{1}$$

where, $M_{0,\tau_{j,i}}$, k, f are respectively the torque preload acting on the joint $\tau_{j,i}$, the equivalent torsional spring stiffness, and an approximation factor controlling the sharpness of the step response. Parameter $\beta_{\tau_{j,i}}$ represents the relative rotation of the joint $\tau_{j,i}$. In Fig. 6 a graph is reported showing the generic response of an ideal preloaded torsional spring along with some approximating functions, in which is changed the hardening factor f. This method allows to consider the complex S-Structure mechanism – which includes internal contacts – as a much more manageable revolute joint with a non-linear rotational spring. Moreover, the complexity reduction and simplification of the model reduces the numbers of DOFs by eight.

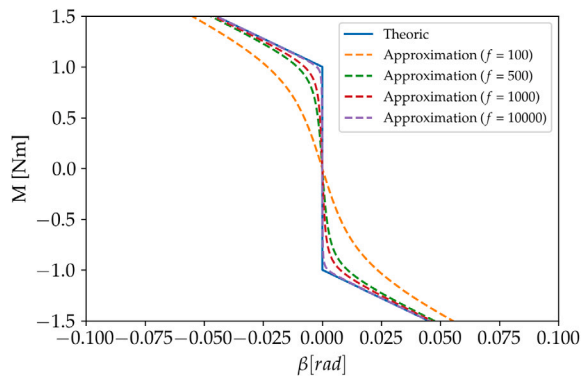

Fig. 6. Step response of a generic ideal preloaded spring (blue solid line) along with the step response approximated function to varying the approximated factor f.

Finally, along with the elastic springs torques, viscus torsional dampers described by the coefficients $c_{\tau_{j,i}}$ have been modeled, which from now on takes the name of c_q since it will be the same for each torsional damper. These provide the damping action which has been seen to occur in the S-Structure, a complex phenomenon that is likely due to internal impacts and frictions [19].

2.2.1. *Dynamics with Kane's method*

In this paragraph the Kane method is outlined, which is used to compute the equations of motions of the overall MBS. This approach, developed by Kane [23], is used to compute the *Equations Of Motion* (EOMs) for complex MBS. Despite the canonical Euler–Lagrange formulation, it allows for faster computation of the equations of motion.

In the method two terms are computed: the generalized inertia forces F^* and the generalized active forces F. Following the D'Alambert principle, the sum of these contributions must be equal to zero. Consider a complex MBS composed by N_b bodies and having n DOFs, the Kane's dynamics equations are described as,

$$F_r + F_r^* = 0, \qquad r = 1, \dots, n \tag{2}$$

according to [23], the two terms are computed as follows,

$$F_r = \sum_{j=1}^{N_b}\left(\frac{\partial \boldsymbol{v}_j}{\partial q_r}\cdot\boldsymbol{F}_j + \frac{\partial \boldsymbol{\omega}_j}{\partial q_r}\cdot\boldsymbol{M}_j\right) \tag{3}$$

$$F_r^* = -\sum_{j=1}^{N_b}\left(\frac{\partial \boldsymbol{v}_j}{\partial q_r}\cdot m_j\boldsymbol{a}_j + \right.$$

$$+\frac{\partial \boldsymbol{\omega}_j}{\partial q_r}\cdot\left(\boldsymbol{I}_j\boldsymbol{\alpha}_j+\boldsymbol{\omega}_j\times\boldsymbol{I}_j\boldsymbol{\omega}_j\right)\Big) \tag{4}$$

where, $\boldsymbol{F}_j$ and $\boldsymbol{M}_j$ are respectively the vectors of the active force and the active moment acting on the jth body, $\boldsymbol{v}_j$ and $\boldsymbol{\omega}_j$ are respectively the linear velocity of the jth body computed in its center of mass; and angular velocity of the jth body about its axis. Moreover, $\boldsymbol{a}_j$ and $\boldsymbol{\alpha}_j$ are respectively the linear acceleration of the jth body computed in its center of mass; and angular acceleration of the jth body about its axis. Finally, m_j and $\boldsymbol{I}_j$ are respectively the body mass and the inertia tensor expressed in the body fixed reference frame.

Eq. (2), results in a system of n *Ordinary Differential Equations* (ODEs) of the second order, which can also be expressed in the most common matrix form.

$$\boldsymbol{M}\ddot{\boldsymbol{q}}+\boldsymbol{C}\dot{\boldsymbol{q}}+\boldsymbol{K}\boldsymbol{q}=\boldsymbol{F} \tag{5}$$

The equations of motions can be expressed in state–space form by introducing an additional state vector such that $\boldsymbol{u}=\dot{\boldsymbol{q}}$. This representation consists of an augmented system of first order ODEs of size $2n$. The result of this process is a linear system of the form,

$$\boldsymbol{A}\dot{\boldsymbol{x}}=\boldsymbol{B}_{rhs} \tag{6}$$

where $\boldsymbol{A}$ is called the mass matrix, $\dot{\boldsymbol{x}}=[\dot{\boldsymbol{q}},\dot{\boldsymbol{u}}]$ is the time derivative of the state vector and $\boldsymbol{B}_{rhs}$ is called the forcing vector and represent the right hand side term of the system. The mass matrix depends only on the generalized coordinates $\boldsymbol{q}$, while the right hand side term, which includes also the Coriolis term, depends both on the generalized coordinates $\boldsymbol{q}$ and its time derivatives $\dot{\boldsymbol{q}}$. The system in (6), is a system of 2n ODEs of the first order, and can be easily time integrated with any integration schema. In this case we used an explicit Runge–Kutta schema of order 5(4), as a trade off between accuracy and computational effort.

2.2.2. Ground contact model

In this context we have modeled the soil as a hard and elastic medium together with a dry friction model. The same is assumed for the wheel. Consequently, since both the soil and the wheel can be considered as hard bodies, the contact between the bodies can be considered as a point contact. Based on these assumptions, the wheel grousers have no effect on the model. Additionally, more than one distinct contact points could exist at any one moment, depending on the geometry of the ground. In the contact point, two forces act on the system: the normal contact force and the friction force.

The first is described by a *Kelvin-Voigt* non-linear spring damper module between each wheel and the ground, whose expression is as follows,

$$F_n=-k_g p^{\sigma}-c_g\dot{p} \tag{7}$$

where, p is the wheels penetration into the ground, $\dot{p}$ the speed of penetration, σ is the coefficient taking care of the non-linear behavior of the spring, k_g is the ground stiffness coefficient and c_g is the ground damping coefficient.

The second, instead, is modeled as described by Makkar et al. in [45] as a continuous and differentiable function, depending on the relative speed between the moving bodies. The model is defined as follows,

$$\begin{aligned}F_k(\dot{q})=\gamma_1\left[\tanh\left(\gamma_2\dot{q}\right)-\tanh\left(\gamma_3\dot{q}\right)\right]\\+\gamma_4\tanh\left(\gamma_5\dot{q}\right)+\gamma_6\dot{q}\end{aligned} \tag{8}$$

where γ_i are positive constants which allow to synthesize a general friction model including: static friction, dynamic friction, Stribeck effect and a dissipation term. In this case the expression describes not the force, but the friction coefficient. The friction coefficient is then used to compute the punctual friction force, using the previously computed normal force.

In order to simplify the model defined in (8), we define the friction model by supplying more meaningful engineering parameters such as the static friction coefficient μ_s, the stiction transition velocity v_s, i.e. the velocity at which the friction coefficient is the static one, the dynamic friction coefficient μ_k, and the friction transition velocity v_k, i.e. the velocity at which the coefficient becomes dynamic. The friction model is then synthesized and the γ_i parameters of (8) are obtained by using a *Dual-Annealing algorithm*.

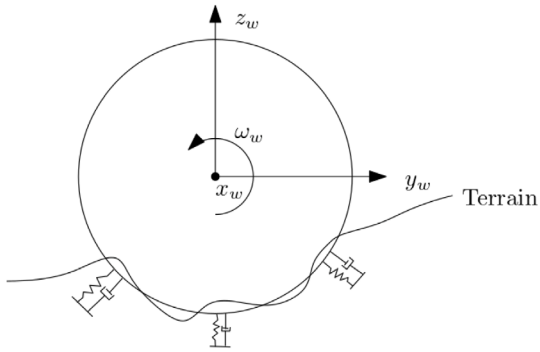

Fig. 7. Bi-dimensional view of the wheel–terrain interaction modeling as a multi point contact. On each contact region a spring–damper system is acting between the soil and the wheel.

The normal contact force and the friction force are not directly included in the computation of the equations of motion with the Kane's method. They are instead added, as generalized forces, directly to the right hand side of the system. These generalized forces are computed as follows,

$$\boldsymbol{Q}_i=\boldsymbol{F}_i\cdot\frac{\partial \boldsymbol{v}_p}{\partial \dot{\boldsymbol{q}}} \tag{9}$$

Since, due to the morphology of the terrain, the wheel may have multiple contact areas, a multi-point contact approach has been adopted. In particular, referring to Fig. 7, for each of the contact area, the contact centroid is computed, and to each a generalized force, is applied, as defined in (9).

A low value of stiffness for the ground k_g is elected to be used in order to take into considerations the elasticity of the wheels and the structural yield of the legs of the rover, which is not explicitly captured by the model. The parameters chosen for the ground contact interface, together with the geometrical and physical ones describing the semi-analytical model are reported in Table 1.

2.2.3. Terrain definition

The terrain over which the rover shall be able to travel, is defined either by assigning its elevation point-by-point over a bi-dimensional grid, or with a set of control points representing the level surface. In the latter method, the points are then interpolated on the bi-dimensional grid, in order to extract the terrain elevation map. The generated terrains are then saved into a convenient *.json* file and loaded at simulation startup; the environment then creates a bi-dimensional grid and an interpolating function which will be constantly used for the wheel–soil interaction algorithm; this detects the contact regions and computes the contact forces.

3. Validation campaign

Our aim is to validate the previously described model, which from now on will be called semi-analytical (SA) model. Indeed, the approach is not perfectly analytical since the exact dynamics equations of the analytical model are integrated numerically using a RK4 integration scheme. The validation is performed both against a commercial dynamics simulator (MSC Adams), and against experimental data. In this section the modeling in Adams of the full MBS representing the

Table 1
Summary of the most representative physical and geometrical parameters chosen, which describe the analytical model of the simplified rover prototype, and the wheel–soil contact interface.

Parameter	Value	Parameter	Value	Parameter	Value
m_R	1.267 kg	d_{j,w_y}	0.168 m	g	9.81 N m s^{-2}
m_{SA}	0.174 kg	d_{j,w_z}	−0.033 m	k_q	9.91 N m rad^{-1}
$m_{j,1}$	0.079 kg	$R_{j,w}$	0.085 m	f	1×10^4
$m_{j,2}$	0.393 kg	$M_{0,\tau_{1,1}}$	1.924 ± 0.039 N m	c_q	0.14 N m s rad^{-1}
$m_{j,w}$	0.231 kg	$M_{0,\tau_{1,2}}$	1.336 ± 0.046 N m	k_g	1×10^6 N m^{-1}
Δ	13.818°	$M_{0,\tau_{2,1}}$	2.096 ± 0.089 N m	c_g	1×10^2 N s m^{-1}
$L \times W$	0.720 m × 0.443 m	$M_{0,\tau_{2,2}}$	1.221 ± 0.031 N m	μ_s	0.3
l_{SA}	0.111 m	$M_{0,\tau_{3,1}}$	1.725 ± 0.069 N m	μ_k	0.2
$l_{j,1}$	0.100 m	$M_{0,\tau_{3,2}}$	1.480 ± 0.053 N m	v_s	5.5×10^{-4} m s^{-1}
$l_{j,2}$	0.169 m	$M_{0,\tau_{4,1}}$	2.048 ± 0.075 N m	v_k	2×10^{-3} m s^{-1}
d_{j,w_x}	0.089 m	$M_{0,\tau_{4,2}}$	1.117 ± 0.032 N m	σ	1.8

Archimede rover is briefly described. Moreover, the setup of the numerical simulations is presented. Subsequently the setup of the experimental campaign is described. Finally, both numerical and experimental results are reported and compared.

3.1. Tests definition

In order to perform the comparison between the SA model, the full model in Adams and the experimental prototype, two main case studies are considered in this work. These are:

- **Case 1: Drop test.** In this case the rover is made to fall from a fixed height with respect to the ground. The rover, subject only to the gravitational acceleration, impacts with the underlying terrain. Within this case two different initial configurations for the rover are considered: an almost horizontal attitude and a highly skewed one. For these cases we present the comparison between the SA model, the Adams full model and the experimental results.
- **Case 2: Obstacle negotiation.** In this second case the rover is made to drive along the horizontal ground. An obstacle is positioned in front of the right bogie, such that all the DOFs of the rover are stressed in a different way. The shape of the obstacle is chosen to be a trapezoid of height 0.1 m, width 0.3 m and a slope angle of 20° with sharp edges. In contrast with the previous case, the comparison is done only between the two simulated models. Within this case, three different rover driving speeds are considered: low speed (0.34 m s^{-1}) and two high velocities (1 m s^{-1} and 2 m s^{-1}). The rover speed is ensured by actively controlling each wheel rotation speed.

3.2. Adams simulated test bed

The modeling of the rover Archimede in Adams, and the numerical simulation setup are presented in this paragraph. The simulation environment, which can be seen in Fig. 8(a), is constituted of the rover MBS, the ground geometry and contact model. Within the Adams simulation environment, the rover Archimede is constructed first by importing each CAD element, which are all developed in SolidWorks (Fig. 1). Subsequently, every imported part is then connected with each other accordingly through appropriate joints. In order to simplify and reduce the computational burden, only the functional parts are kept while the others are considered inside the physical parameters of the former.

On the other hand the terrain is modeled as a large rigid box having dimensions $(20 \times 20 \times 0.5)\text{m}^3$, to which at the top are merged some modeled obstacles. External loads are mainly: the gravitational acceleration acting on the rover MBS; inside each S-Structure module a linear preloaded spring and two contact forces are defined, in order for the contiguous modules to not compenetrate; finally between each wheel and the ground a set of possible contact forces are defined. Summing up, the Adams simulation environment is composed by 32 bodies, 32 joints and 29 forces.

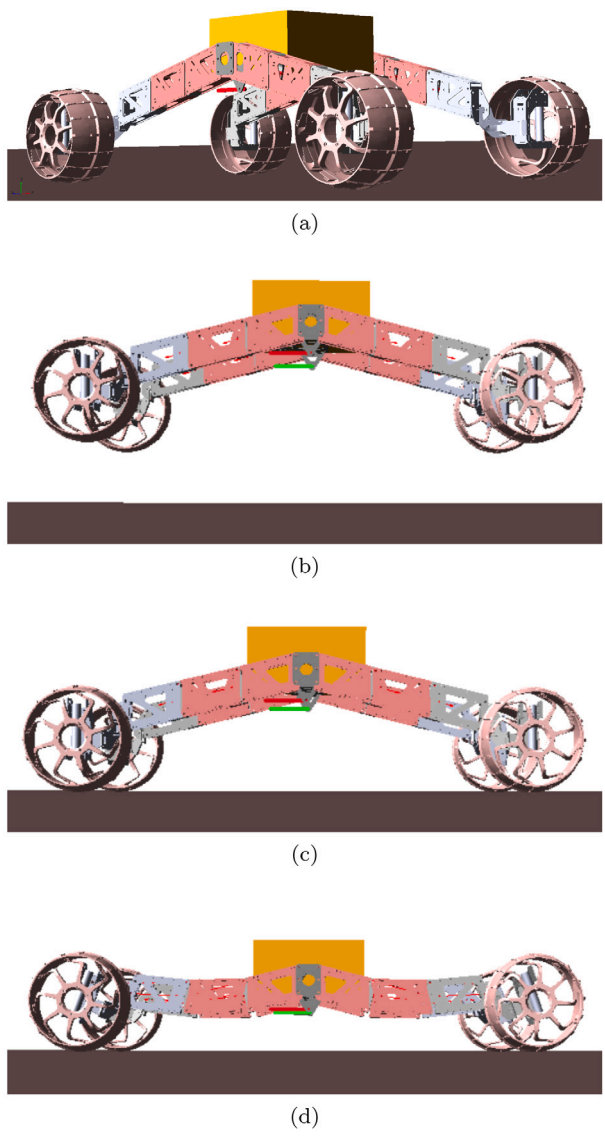

Fig. 8. In (a) the CAD model of the Archimede rover imported in the Adams simulation environment and simplified by relieving it from the non functional parts. Snapshots of the rover configurations in the different phases of the impact simulation over a horizontal surface in Adams: in (b) the initial condition; in (c) the moment of touchdown with the pavement; in (d) the moment of maximum deflection of the overall system.

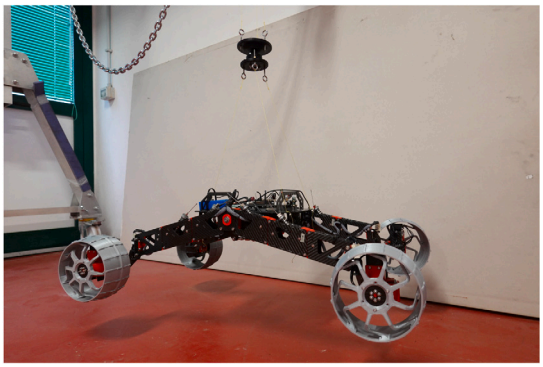

Fig. 9. Experimental setup for the rover prototype drop test.

Table 2
Initial conditions of the rover used in the three models for the horizontal and skewed drop test.

Type	z [m]	χ [rad]	ψ [rad]
Horizontal	0.281	0.039	0.0042
Skewed	0.299	0.116	−0.0809

3.3. Experimental testbed

In order to have an accurate representation of the experimental testbed in the simulations, the preload of the linear springs composing the S-Structure was measured. For this reason, a load cell was used in order to measure the first detachment tension. The measured springs preload, converted into moment preload $M_{0,\tau_{j,i}}$ are reported in Table 1.

The experimental setup for the drop test is shown in Fig. 9. The rover is attached with cables to a 3D printed release mechanism, fabricated with POM, a low friction material. The overall system is then suspended by a gantry crane, and the inclination of the rover body is adjusted acting on the screws, with the support of an appropriate calibrated inertial measurement unit (IMU). In order to capture the structure movement, a high frame rate camera has been used; the complete acquisition system suite chosen is RDI Motion Amplification; preliminary analysis was performed using a SONY RX100 VII.

3.4. Results

In this section, for each of the two cases previously illustrated, the results for the three rover models (SA, Adams and experimental), are presented. The physical and geometrical parameters of the models are reported in Table 1.

In order to provide a meaningful way of comparing the numerical results of both methods with the experimental campaign results, we provide a series of indices to quantify the deviation in each test. The main aspects we analyze are the dynamical behavior of the rover in a drop test, i.e. during a sudden impact with the ground, and during obstacle negotiation, where a small asymmetrical trapezoidal obstacle is driven over by the rover. The indices quantify the relative error between the two numerical models and the experimental prototype.

3.4.1. Drop test

As previously reported, for this case test, the models that are compared are the semi-analytical, the Adams and the experimental ones. In order to compare the three models under study, the same initial conditions of the rover must be used. These conditions, which concerns the drop height, the pitch and roll angles, are reported in Table 2 for both the horizontal and skewed drop tests.

Figs. 8(b), 8(c) and 8(d) represent graphically, for the case of a sample horizontal drop test in Adams, respectively the initial configuration of the rover, the moment it touches the ground and the moment at which the structure experiences maximum deflection.

In Fig. 10 we report some acquired frames, with the high frame rate camera, obtained during the experimental drop tests conducted on the rover prototype. Specifically, the first row (a–d) represent the horizontal drop; while the second row (e–h) represent the skewed drop. For each row, the frames from the left to the right represent respectively the initial configuration of the rover, the moment the wheels touch the ground, the moment of maximum deflection and the "at rest" state.

Finally, results in terms of vertical displacement of the pin of the left bogie of the rover are reported in Figs. 11(a) and 11(b).

In order to numerically quantify the errors, we define the *deflection error*, as follows,

$$\epsilon_{d,*} = \frac{z_{r,*} - z_{min,*}}{z_{r,EXP} - z_{min,EXP}} - 1 \tag{10}$$

where $z_{min,*} = min(\mathbf{B}_{l,*}|_z)$ and $z_{r,*} = \mathbf{B}_{l,*}|_z(t = 1s)$ and $*$ is the data source, i.e. semi-analytical (SA) numerical (Adams) or experimental (EXP). With the same nomenclature, we can define the error for the "*at-rest*" configuration, after impact motion has ceased, as follows,

$$\epsilon_{r,*} = \frac{\mathbf{B}_{l,*}|_z}{\mathbf{B}_{l,EXP}|_z} - 1 \tag{11}$$

To summarize, we define two metrics for the quantitative comparison between the models: the *deflection error* and the *at-rest error*. The former is related to the impact-caused deflection of the chassis of the rover with respect to the ground, while the other is related to the sag of the rover after motion has ceased. These indices will be used in the following to characterize these aspects of the performance of the models, allowing for a comprehensive comparison and evaluation.

3.4.2. Obstacle negotiation

In contrast to the previous case, in this case only the SA and Adams models are considered and compared. Again, in order to be able to compare the two models, these shall have the same initial conditions. In this case these are the position in the environment and the initial velocity.

In Fig. 12(a) we show the configurations of the rover for the case of speed $1\,\mathrm{m\,s^{-1}}$. The rover is described by the SA model, with the right wheel on the top of the obstacle, intent on its negotiation. In Fig. 12(b), on the other hand, the same rover configuration is shown instead with the Adams model.

In the following we present the results for both the models, in terms of vertical displacement of three points characteristic to the rover; precisely we show the left bogie pin ($\mathbf{B}_l$), the right bogie pin ($\mathbf{B}_r$) and the rover center of mass ($\mathbf{G}$) in Fig. 11(c–e). The prefix A indicates the Adams model, while the prefix SA the semi-analytical one. In particular, Figs. 11(c), 11(d) and 11(e) reports respectively the vertical displacement of the three points for the rover speed of 0.34, 1 and 2 $\mathrm{m\,s^{-1}}$.

Finally, results in terms of pitch and roll angles of the rover models are reported in Fig. 11(f–h). Again, Figs. 11(f), 11(g) and 11(h) report respectively the pitch and roll angles evolution within both the rover models, for a rover speed of 0.34, 1 and 2 $\mathrm{m\,s^{-1}}$.

A series of indices are defined as metrics to evaluate the discrepancy between the models, in this case the SA and ADAMS models. In particular, we define $RMS_{\mathbf{B}_l|_z}$ and $RMS_{\mathbf{B}_r|_z}$, the *Root Mean Square* (RMS) error between the position of the point $\mathbf{B}_r$ and $\mathbf{B}_l$ – the "hips" – in the SA and ADAMS models. For the position of the barycenter, we use $RMS_{\mathbf{G}|_z}$, while for the pitch and roll angles respectively RMS_χ and RMS_ψ.

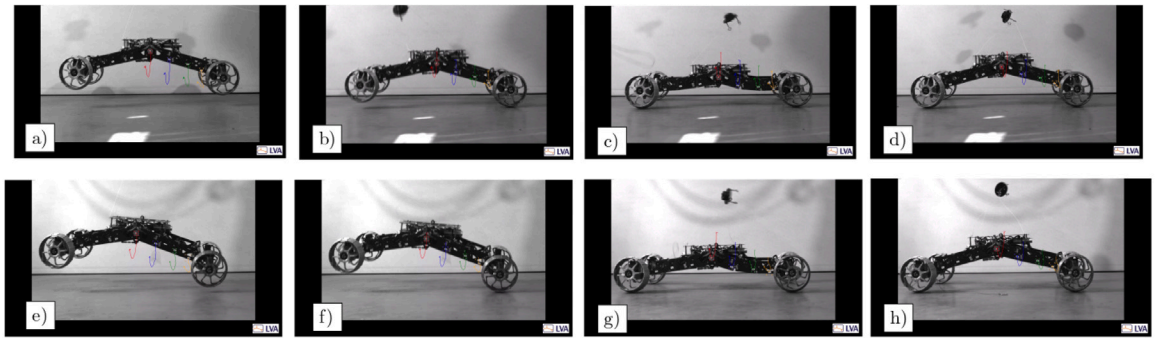

Fig. 10. Time-series frames of the two experimental drop tests: in the top row the drop test on the horizontal surface; in the bottom row the skewed drop. For both rows the figures in the first column (a and e) represent the initial configuration of the rover; in the second (b and f), the moment of first impact with the ground; in the third (c and g), the moment of maximum displacement of the legs of the rover; in the last (d and h), the final "rest" configuration.

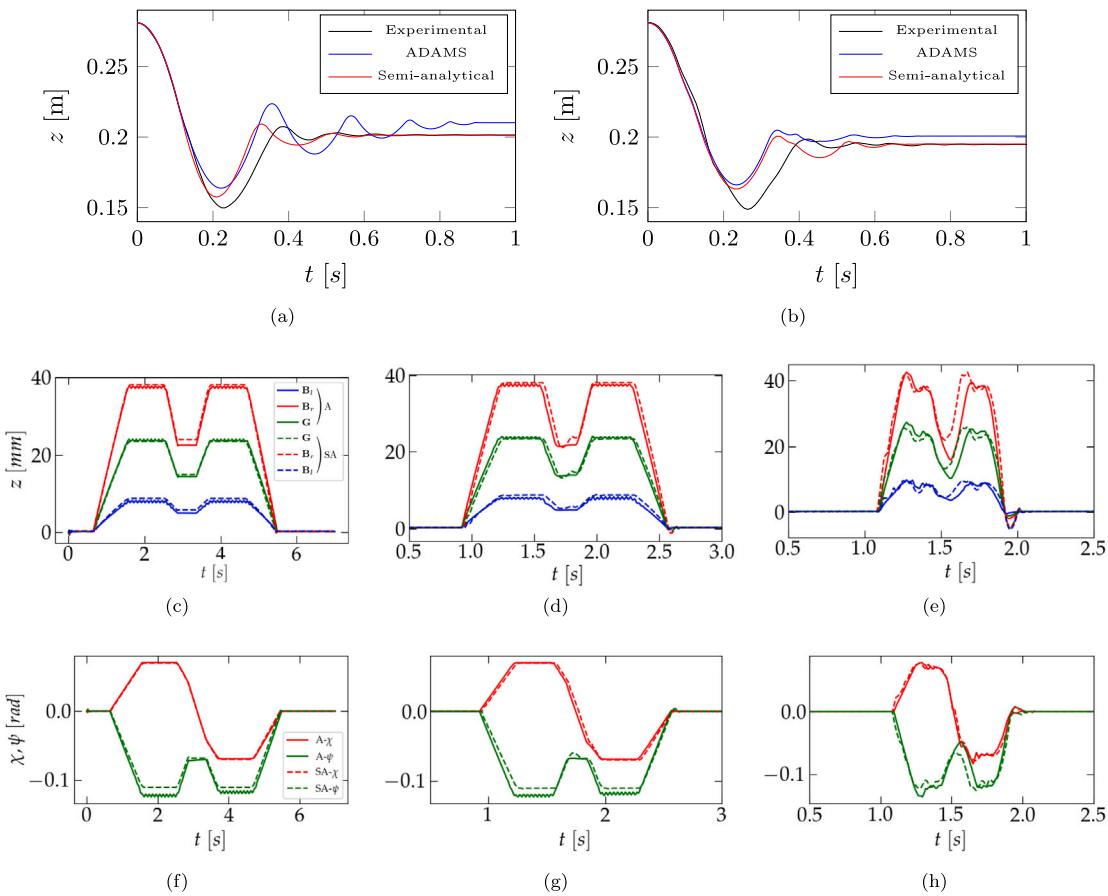

Fig. 11. In the top row the vertical displacement of the pin of the left bogie of the rover for each of the three models, for the cases of: horizontal drop test (a) and the skewed drop test (b). In the middle row the vertical displacement of the left bogie pin ($\mathbf{B}_l$), the right bogie pin ($\mathbf{B}_r$) and the rover center of mass ($\mathbf{G}$) for the rover longitudinal speed of: 0.3 (c), 1 (d) and 2 (e) $\mathrm{m\,s^{-1}}$. In the bottom row the trend of the rover pitch and roll angles for the SA and Adams models for the rover longitudinal speed of: 0.3 (f), 1 (g) and 2 (h) $\mathrm{m\,s^{-1}}$.

3.5. Sensitivity analysis

In order to quantify the effects of uncertainty of some parameters of the semi-analytical model, to tune parameters and to better fit it with the experimental one, in this section we perform a sensitivity analysis varying a subset of parameters, such as f and c_q and the torque preload $M_{0,\tau_{j,i}}$.

In particular, the Root Mean Square (RMS) error between the experimental curves and the simulated ones is chosen as a metric. The main parameter to tune is the damping coefficient c_q of the equivalent joints, in order to better approximate the damping effect introduced in the real S-Structure. For this reason a large number of simulations has been conducted, for the case of horizontal drop test. In these simulations, every variable subject to the uncertainty reported above, is made to vary randomly.

With reference to Fig. 6, ideally, in order to better represent the step response of the preloaded springs of the generic S-Structure, it is desirable that $f \longrightarrow \infty$. On the other hand, large values of this parameter increase joint dynamics discontinuities, which affects negatively the solver performances. The study shown in Fig. 13(a) aims at providing a quantitative value of this influence. It can be seen that the computational time t_c needed to complete a simulation increases linearly. From the same figure it can also be seen that the RMS presents a minimum for comparably low values of f, and then tends to increase

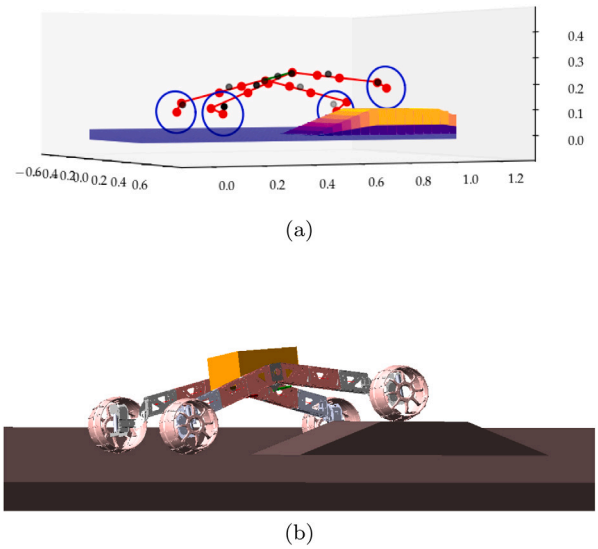

Fig. 12. In (a) a snapshot of the rover overcoming the ramp obstacle in the simulation conducted in python; in (b) the same simulation conducted in Adams.

linearly. This behavior is most likely due to several diverse aspects: backlashes are present in the generic S-Structure; the steel cables are elastic; the coupling between cable and module is implemented through a loop in the cable. All these elements combined lead to the fact that the preload spring response follows a smoother trend compared to the expected step response, which it can be speculated to be better described by using low values of f.

Another fascinating result is obtained by varying both the variables c_q and f at the same time, and is reported in Fig. 13(b) and in Fig. 13(c). The former shows the response surface describing the RMS by varying both f and c_q. It can be seen that low values of RMS are reached for either low values of c_q and any of f or low values of f and c_q. However, since we want to better represent the step response of the linear preloaded spring inside the S-Structure (with f equal to 1×10^4), we have elected to use a low value of c_q, in this case equal to $0.14\,\mathrm{N\,m\,s\,rad^{-1}}$. The latter, instead, shows the response surface describing the computation time t_c by varying both f and c_q. It can be seen that computation time increases when f and c_q increases.

Finally, chosen the values for the hardness of the step response f and the torsional damping coefficient c_q, we quantified the influence of the uncertainty of the determination of the single torque preload $M_{0,\tau_{j,i}}$. In particular, many runs are conducted choosing for each joint a random torque value inside its normal distribution, which has been determined experimentally and reported in Table 1. The result of these variations is reported in Fig. 13(d). More precisely, the plot shows the indeterminacy of the vertical position in z of the left pin of the rover (in close proximity to $\mathbf{B}_l$), due to the measurement uncertainty of the preload torques $M_{0,\tau_{j,i}}$; the figure shows the distribution as a gradient, along with a 3σ confidence interval.

4. Discussion

In this section the results reported in the previous section for the two case studies are discussed in detail. The sources of uncertainty are first listed and discussed, then, a detailed analysis is given of the results proper, with comparisons between the three models.

The rover presented in this work is a very complex machine; it has a large number of DOFs and parameters, factors which inevitably increase the overall complexity. This makes it very hard to model and to reproduce its dynamics while interacting with the environment. Moreover, in the prototype, a large number of sources of uncertainty exist: backlash in the joints of the S-Structure and flexibility of the structure; these aspects in particular cause the legs to twist axially during impact. A small uncertainty is present in the determination of the preload tension of the springs and in the values of the spring stiffnesses. Furthermore, liability has been observed in the steering hub; in fact, during impact on the ground, the wheels tend to rotate around their steering axis, suggesting the presence of a compliant phenomenon in the steer joint; the wheel hub and rims also tends to flex. An additional source of experimental uncertainty can be found in the release mechanism used to initiate the drop. In particular, despite being designed and fabricated to minimize interference, when the release mechanism is actuated, a small perturbation is introduced in the system, thus on the initial conditions of the rover in the drop test cases. Evidence of this effect can be seen in the initial part of the experimental curve in Figs. 11(a) and 11(b).

We underline that for the numerical models, i.e. the semi-analytical and Adams, the solvers that solve the ODEs are different. This can be a source of divergence between the two models, as well.

Finally, a big impact is given by the interaction with the ground. It has been witnessed that during impact with the ground, the wheels experience a rapid succession of bounces; in addition, wheels are subject to a consistent level of play in the rolling axis, due to the comparatively loose coupling with the motor. These two effect combined cause the wheel to be influenced only negligibly by friction during impact and deflection (in Fig. 11(a), from 0.17 s to 0.22 s approximately), but more so during the rebound (0.22–0.35 s), where the wheels are firmly in contact. Essentially, the bounces recuperate the play, meaning that the effect of friction on motion during deflection is much lower. The effect is a higher deflection and lower rebound compared to the other curves which do not suffer from this effect.

All of the above phenomena are captured only in part by the numerical models, which contributes to a certain degree of deviation of the models from the experimental results. However, it is interesting to note that the semi-analytical model shows in general good adherence after the rebound. This is likely due to the fact that we fit the model by changing the value of the damping coefficients c_q of the lumped-parameters S-Structures joints; indeed, these are virtual parameters and do not have a physical counterpart. The Adams model however replicates the S-Structure mechanism which is not fitted with an explicit damping component; the damping observed in the experimental campaign is probably due to the complex behavior of friction with the ground, as explained in the previous paragraph and which is only loosely modeled by Adams. Finally, the semi-analytical model shows remarkable coherency with the experiments in the latter part of the time series, after motion has ceased; on the other hand Adams does not capture this very well. This is likely due to the fact that the experimental model experiences some degree of structural compliance which is captured very well by the semi-analytical model through its soft description of the elastic response, as per Eq. (1).

If we take into considerations the definition for the errors in Eqs. (10) and (11), despite the described inaccuracies and the difference in the transient phase, the models show good adherence in the rest state. This is especially true of the semi-analytical and the experimental comparison. Indeed, taking Table 3 as reference, we can see that the errors are quite low at rest configuration for the horizontal drop for the semi-analytical approach. The numerical model shows higher error values; if we take into consideration the error at rest, with errors as low as $\varepsilon_{r,SA} = 0.2\%$ for the skewed drop. Errors for the maximum deflection are considerably higher, reaching a maximum of $\varepsilon_{d,Adams} = 24.8\%$ in the Adams model, and $\varepsilon_{d,SA} = 30.9\%$ in the SA model in case of skewed drop. These deflection error values for the skewed case are attributable in part to all the causes previously described, such as presence of backlash, friction and structural compliance. Moreover, to the difficulty in recreating the initial conditions for the numerical models that match those of the experimental setup. Finally, it must be remembered that for the skewed case the measurement plane on the rover is inclined

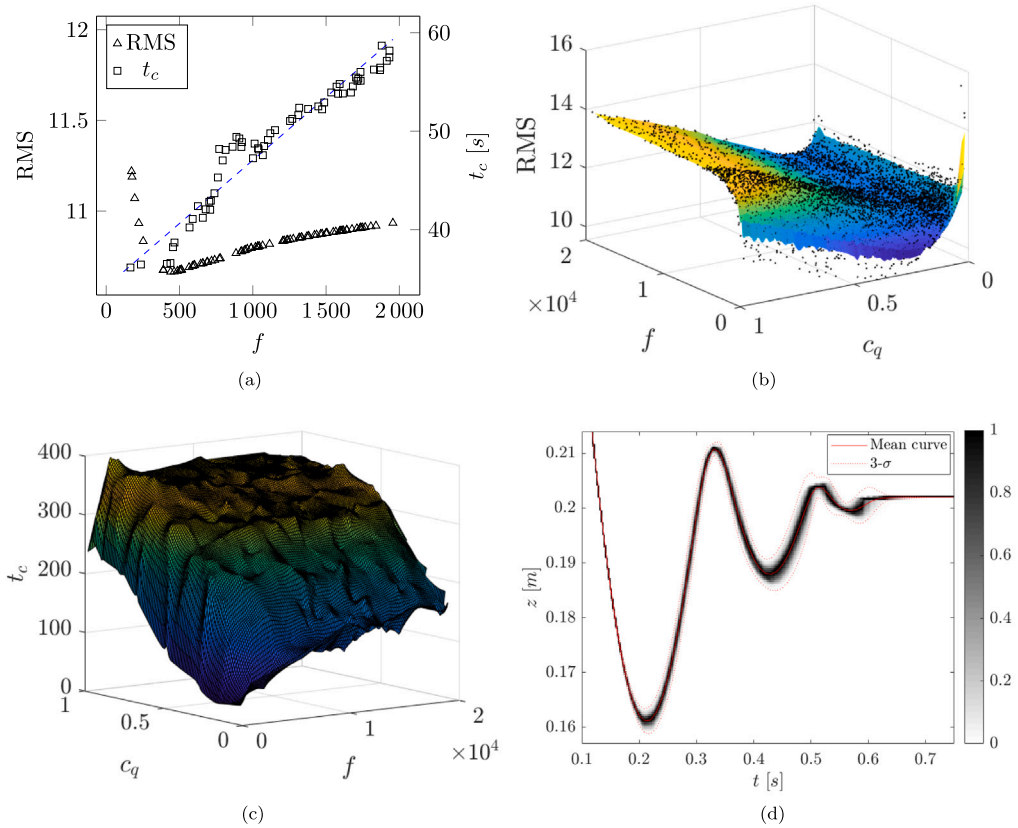

Fig. 13. In (a) the influence of the parameter f on the computation time t_c in seconds and on the RMS (in mm), together with linear regression for the computation time; in (b) the response surface describing the RMS as the parameters f and c_q (in $\mathrm{N\,m\,s\,rad^{-1}}$) vary; in (c) the response surface describing the computation time t_c; and in (d) influence of the variation of the torque preloads $M_{0,\tau_{j,l}}$ in N m on the vertical displacement of the pin of the left bogie: here, the fuzziness represents a normalized statistical distribution associated with an uncertain value of $M_{0,\tau_{j,l}}$, together with its mean value and 3σ boundaries.

with respect to the one of the Motion Amplifier sensor with consequent errors of accuracy in the identified displacements. All these factors combined introduce errors, which are reflected in a higher deflection error than in the horizontal drop case.

For what concerns the drive tests, with reference to Fig. 11(c–h), it can be seen a remarkable adherence between the responses of the two considered models, i.e. the semi-analytical and the Adams ones. However some considerations about these results must be made. In particular from Fig. 11(f–h), it can be seen that the pitch angle between the models match perfectly, but the trend of the roll angles present little differences. The source of these differences can be found in the fact that in the Adams model the wheels are rigid bodies with depth extension, in contrast to those of the SA model which are modeled as a disk with no depth. As such, when the rover meets and tries to overcome the obstacle, it rigidly tilts; this causes the contact patch to change all along the wheel profile as the roll angle increases, and the distance between the wheel axle and the contact point increases as well. This is the reason why with the same simulation time the roll angle in the Adams model is greater than the semi-analytical one.

Since the position of the three considered points ($\mathbf{B}_l|z$, $\mathbf{B}_r|z$ and the center of mass $\mathbf{G}|z$) depend on the roll angle, the difference between the roll angles influences the vertical displacement of the pins, in particular it is slightly lower than the ones described by the SA model, and can be seen in Fig. 11(c-e).

An interesting consideration, which can be noted in particular in Fig. 11(c,d,f,g), is that the solid curves, at the top of their trapezoid shape, present oscillations at higher frequency. This is due to the fact that the rover is so tilted that, the wheel contact patch is located on its grousers. This way, when the contact patch moves from a grouser to the next one, the rover experiences a hopping motion.

If we look carefully at Fig. 11(d,e,g,h), we can see that the curves of the Adams and the SA models are slightly shifted in time. Given the way contacts are modeled, they implicitly assume that the wheels always work in slip conditions. Contact between the models are different, especially because of friction. For this reason the wheels between the two models are subject to different slip magnitudes. This difference inevitably translates into the punctual velocity of the rover and in its traveled distance.

Finally, for the rover speed of $0.34\,\mathrm{m\,s^{-1}}$, the curves reported in Fig. 11(c,f), basically follows the shape of the obstacle, thus suggesting the dynamics effects are very small. For the case of the rover speed of $1\,\mathrm{m\,s^{-1}}$, Fig. 11(d,g), the shape of the obstacle can still be clearly recognized, however dynamics effect starts to be visible in some points. For the case of $2\,\mathrm{m\,s^{-1}}$, Fig. 11(e,h), on the other hand, the dynamic effects distort the trajectory compared to the obstacle shape. In these curves the moments can be clearly recognized at which the wheels are not in contact with the ground, the bounces and the rebounds of the structure.

We note, however, that even for the high speed cases (1 and $2\,\mathrm{m\,s^{-1}}$), adherence between the two selected models is kept under control for the most part. These two speeds are characterized on including high dynamics effects, since the speed reached by the rover during the drop test is comparable.

In order to provide a quantitative idea about the adherence between the two models, the RMS between the curves of the Adams model and the semi-analytical ones, is computed for all the simulations cases. We can see from Table 3, that the values are considerably low for the roll and pitch angles, with maximum values around 0.007 rad, and no larger than 3 mm in the case of the $\mathbf{B}_l|z$ and $\mathbf{B}_r|z$.

Table 3
Comparison between semi-analytical (SA) and numerical (Adams) models and experimental (EXP) errors for the two case studies. Drop test: "*at-rest*" error for SA and the Adams models with respect to EXP; deflection error for SA and Adams models with respect to EXP. Drive test: the RMS between the SA and Adams models.

Drop tests			Drive tests		
$\varepsilon_{r,SA}$	(horizontal)	0.7%	$RMS_{\mathbf{B}_{\|z}}$	($v = 0.34$ m s^{-1})	0.6042 mm
	(skewed)	0.2%		($v = 1$ m s^{-1})	0.5525 mm
$\varepsilon_{r,Adams}$	(horizontal)	5.1%		($v = 2$ m s^{-1})	0.9335 mm
	(skewed)	3.1%	$RMS_{\mathbf{B}_{r\|z}}$	($v = 0.34$ m s^{-1})	0.7457 mm
$\varepsilon_{d,SA}$	(horizontal)	12.6%		($v = 1$ m s^{-1})	1.1962 mm
	(skewed)	30.9%		($v = 2$ m s^{-1})	2.6094 mm
$\varepsilon_{d,Adams}$	(horizontal)	7.57%	$RMS_{\mathbf{G}_{\|z}}$	($v = 0.34$ m s^{-1})	0.4440 mm
	(skewed)	24.8%		($v = 1$ m s^{-1})	0.7007 mm
				($v = 2$ m s^{-1})	1.5758 mm
			RMS_{χ}	($v = 0.34$ m s^{-1})	0.0012 rad
				($v = 1$ m s^{-1})	0.0032 rad
				($v = 2$ m s^{-1})	0.0035 rad
			RMS_{ψ}	($v = 0.34$ m s^{-1})	0.0068 rad
				($v = 1$ m s^{-1})	0.0057 rad
				($v = 2$ m s^{-1})	0.0072 rad

5. Conclusion

In the present work a novel four steerable wheel rover for space exploration is presented, which is based on the use of complex compliant joints called S-Structures. A semi-analytical model of the rover dynamics is derived by using Kane's method. The model condenses the complex S-Structure mechanism in a simple revolute joint with preloaded non-linear elastic response, thus allowing us to reduce the complexity of the system. Within this work, two additional distinct models are presented: one based on Adams, and an experimental prototype. All models are compared numerically and experimentally, and results have shown that, despite the many sources of inaccuracies, there is good adherence between the models, especially between SA and the experimental. Indeed, results show that the behavior of the proposed rover can be well described by the SA model; furthermore, they demonstrate how a complex system as the S-Structure can be reduced and simplified with an equivalent preloaded revolute joint.

From the discussion of the results and the comparison between the various models, it emerges how using the SA model can be beneficial in terms of accuracy compared to reality, and in terms of complexity of computation; indeed, the SA model is considerably less complex than the one developed in Adams, which has considerably more moving parts – hence DOFs – and internal contacts. These contacts, specifically, in order to be representative, require careful measurements of the actual mechanics of contact of the physical counterpart. The SA approach enables us to effectively aggregate these complex effects in a pair of parameters, namely c_q and f, making the model more flexible and easy to implement.

In this direction, future work foresees the implementation of the rover and its semi-analytical model in a more complex scenario; for example a scenario constructed from celestial bodies surface observations; i.e. with rocks, craters and hills. Given the limitations of the rigid soil model employed in this study, in order to better represent the behavior on the soft soils which occur in many planetary environments, terramechanics based models will be adopted, e.g. the Bekker model [31]. In this context the behavior of the rover will be studied in detail and compared with appropriate experiments on real soft soil, e.g. lunar simulants based on volcanic basaltic rock.

Funding

This work has been partially supported by the PRIN project "SEDUCE" n. 2017TWRCNB of the "Ministero dell'Istruzione, dell'Universitá e della Ricerca" (MIUR), Italy, and by the internal funding program "Microgrants 2020" of the University of Trieste, Italy.

CRediT authorship contribution statement

Matteo Caruso: Writing – original draft, Writing – review, Methodology, Software, Numerical simulation, Data curation, Validation. **Luigi Bregant:** Data curation, Experimental campaign, Writing - review. **Paolo Gallina:** Writing - review, Project supervision. **Stefano Seriani:** Conceptualization of the study, Validation, Writing – review, Project supervision, Funding acquisition.

Declaration of competing interest

The authors declare that they have no known competing financial interests or personal relationships that could have appeared to influence the work reported in this paper.

Data and code availability

Data are provided by the authors upon reasonable request.

References

[1] J. Grotzinger, J. Crisp, A. Vasavada, R. Anderson, C. Baker, R. Barry, D. Blake, P. Conrad, K. Edgett, B. Ferdowski, R. Gellert, J. Gilbert, M. Golombek, J. Gómez-Elvira, D. Hassler, L. Jandura, M. Litvak, P. Mahaffy, J. Maki, M. Meyer, M. Malin, I. Mitrofanov, J. Simmonds, D. Vaniman, R. Welch, R. Wiens, Mars science laboratory mission and science investigation, Space Sci. Rev. 170 (1–4) (2012) 5–56.

[2] P. Mahaffy, C. Webster, M. Cabane, P. Conrad, P. Coll, S. Atreya, R. Arvey, M. Barciniak, M. Benna, L. Bleacher, W. Brinckerhoff, J. Eigenbrode, D. Carignan, M. Cascia, R. Chalmers, J. Dworkin, T. Errigo, P. Everson, H. Franz, R. Farley, S. Feng, G. Frazier, C. Freissinet, D. Glavin, D. Harpold, D. Hawk, V. Holmes, C. Johnson, A. Jones, P. Jordan, J. Kellogg, J. Lewis, E. Lyness, C. Malespin, D. Martin, J. Maurer, A. McAdam, D. McLennan, T. Nolan, M. Noriega, A. Pavlov, B. Prats, E. Raaen, O. Sheinman, D. Sheppard, J. Smith, J. Stern, F. Tan, M. Trainer, D. Ming, R. Morris, J. Jones, C. Gundersen, A. Steele, J. Wray, O. Botta, L. Leshin, T. Owen, S. Battel, B. Jakosky, H. Manning, S. Squyres, R. Navarro-González, C. McKay, F. Raulin, R. Sternberg, A. Buch, P. Sorensen, R. Kline-Schoder, D. Coscia, C. Szopa, S. Teinturier, C. Baffes, J. Feldman, G. Flesch, S. Forouhar, R. Garcia, D. Keymeulen, S. Woodward, B. Block, K. Arnett, R. Miller, C. Edmonson, S. Gorevan, E. Mumm, The sample analysis at mars investigation and instrument suite, Space Sci. Rev. 170 (1–4) (2012) 401–478.

[3] M. Lapotre, R. Ewing, M. Lamb, W. Fischer, J. Grotzinger, D. Rubin, K. Lewis, M. Ballard, M. Day, S. Gupta, S. Banham, N. Bridges, D. Marais, A. Fraeman, J. Grant, K. Herkenhoff, D. Ming, M. Mischna, M. Rice, D. Sumner, A. Vasavada, R. Yingst, Large wind ripples on mars: A record of atmospheric evolution, Science 353 (6294) (2016) 55–58.

[4] C. Webster, P. Mahaffy, S. Atreya, J. Moores, G. Flesch, C. Malespin, C. McKay, G. Martinez, C. Smith, J. Martin-Torres, J. Gomez-Elvira, M.-P. Zorzano, M. Wong, M. Trainer, A. Steele, D. Archer Jr., B. Sutter, P. Coll, C. Freissinet, P.-Y. Meslin, R. Gough, C. House, A. Pavlov, J. Eigenbrode, D. Glavin, J. Pearson, D. Keymeulen, L. Christensen, S. Schwenzer, R. Navarro-Gonzalez, J. Pla-García, S. Rafkin, A. Vicente-Retortillo, H. Kahanpää, D. Viudez-Moreiras, M. Smith, A.-M. Harri, M. Genzer, D. Hassler, M. Lemmon, J. Crisp, S. Sander, R. Zurek, A. Vasavada, Background levels of methane in mars' atmosphere show strong seasonal variations, Science 360 (6393) (2018) 1093–1096.

[5] L. Witte, A. Heffels, M. Killian, M. Knapmeyer, C. Lange, N. Toth, G. Tsakyridis, A. Wedler, A robotically deployable lunar surface science station and its validation in a moon-analogue environment, Planet. Space Sci. 193 (2020).

[6] S. Campagnola, C. Yam, Y. Tsuda, O. Naoko, Y. Kawakatsu, Mission analysis for the martian moons explorer (MMX) mission, Acta Astronaut. 146 (2018) 409–417.

[7] S. Seriani, P. Gallina, A. Wedler, A modular cable robot for inspection and light manipulation on celestial bodies, Acta Astronaut. 123 (2016) 145–153.

[8] M. Schuster, M. Muller, S. Brunner, H. Lehner, P. Lehner, R. Sakagami, A. Domel, L. Meyer, B. Vodermayer, R. Giubilato, M. Vayugundla, J. Reill, F. Steidle, I. Von Bargen, K. Bussmann, R. Belder, P. Lutz, W. Sturzl, M. Smisek, M. Moritz, S. Stoneman, A. Prince, B. Rebele, M. Durner, E. Staudinger, S. Zhang, R. Pohlmann, E. Bischoff, C. Braun, S. Schroder, E. Dietz, S. Frohmann, A. Borner, H.-W. Hubers, B. Foing, R. Triebel, A. Albu-Schaffer, A. Wedler, The ARCHES space-analogue demonstration mission: Towards heterogeneous teams of autonomous robots for collaborative scientific sampling in planetary exploration, IEEE Robot. Automat. Lett. 5 (4) (2020) 5315–5322.

[9] A. Wedler, M. Schuster, M. Müller, B. Vodermayer, L. Meyer, R. Giubilato, M. Vayugundla, M. Smisek, A. Dömel, F. Steidle, P. Lehner, S. Schröder, E. Staudinger, B. Foing, J. Reill, German aerospace center's advanced robotic technology for future lunar scientific missions: Dlr's advanced robotic technology, Philos. Trans. R. Soc. A: Math., Phys. Eng. Sci. 379 (2188) (2021).

[10] B. Muirhead, A. Karp, Mars sample return lander mission concepts, in: IEEE Aerospace Conference Proceedings, 2019-March, 2019, URL https://www.scopus.com/inward/record.uri?eid=2-s2.0-85068340074&doi=10.1109%2fAERO.2019.8742215&partnerID=40&md5=ebb71e06e6369ac20afdc34e03197710.

[11] B. Muirhead, A. Nicholas, J. Umland, O. Sutherland, S. Vijendran, Mars sample return campaign concept status, Acta Astronaut. 176 (2020) 131–138.

[12] S. Mallapaty, China has landed its first rover on Mars - here's what happens next, Nature 593 (7859) (2021) 323–324, http://dx.doi.org/10.1038/d41586-021-01301-7, cited By 0.

[13] B. Oglesby, A. Prince, G. Story, A. Kam, Qualification of a hybrid propulsion system for a mars ascent vehicle, in: IEEE Aerospace Conference Proceedings, 2019-March, 2019, URL https://www.scopus.com/inward/record.uri?eid=2-s2.0-85068340943&doi=10.1109%2fAERO.2019.8741599&partnerID=40&md5=7ea1d0ea8c3fa9a6ba2b23299d335bb7.

[14] Y. Tsuda, T. Saiki, F. Terui, S. Nakazawa, M. Yoshikawa, S.-I. Watanabe, H.P. Team, Hayabusa2 mission status: Landing, roving and cratering on asteroid ryugu, Acta Astronaut. 171 (2020) 42–54.

[15] M. Schuster, S. Brunner, K. Bussmann, S. Büttner, A. Dömel, M. Hellerer, H. Lehner, P. Lehner, O. Porges, J. Reill, S. Riedel, M. Vayugundla, B. Vodermayer, T. Bodenmüller, C. Brand, W. Friedl, I. Grixa, H. Hirschmüller, M. Kaßecker, Z.-C. Márton, C. Nissler, F. Ruess, M. Suppa, A. Wedler, Towards autonomous planetary exploration: The lightweight rover unit (LRU), its success in the SpaceBotCamp challenge, and beyond, J. Intell. Robot. Syst.: Theory Appl. 93 (3–4) (2019) 461–494.

[16] F. Vulpi, A. Milella, F. Cordes, R. Domínguez, G. Reina, Deep terrain estimation for planetary rovers, in: 15th International Symposium on Artificial Intelligence, Robotics and Automation in Space, ISAIRAS-2020, October 2020.

[17] S. Seriani, L. Scalera, A. Gasparetto, P. Gallina, Preloaded structures for space exploration vehicles, in: A. Gasparetto, M. Ceccarelli (Eds.), Mechanism Design for Robotics, Springer International Publishing, Cham, 2019, pp. 129–137.

[18] S. Seriani, P. Gallina, A. Wedler, Dynamics of a tethered rover on rough terrain, Mech. Mach. Sci. 47 (2017) 355–361, http://dx.doi.org/10.1007/978-3-319-48375-7_38, cited By 5.

[19] S. Seriani, P. Gallina, L. Scalera, V. Lughi, Development of n-dof preloaded structures for impact mitigation in cobots, J. Mech. Robot. 10 (5) (2018) http://dx.doi.org/10.1115/1.4040632, arXiv:https://asmedigitalcollection.asme.org/mechanismsrobotics/article-pdf/10/5/051009/6375644/jmr_010_05_051009.pdf.

[20] M.J. Schuster, C. Brand, S.G. Brunner, P. Lehner, J. Reill, S. Riedel, T. Bodenmüller, K. Bussmann, S. Büttner, A. Dömel, W. Friedl, I. Grixa, M. Hellerer, H. Hirschmüller, M. Kassecker, Z.-C. Márton, C. Nissler, F. Ruess, M. Suppa, A. Wedler, The LRU rover for autonomous planetary exploration and its success in the SpaceBotCamp challenge, in: 2016 International Conference on Autonomous Robot Systems and Competitions, ICARSC, 2016, pp. 7–14, http://dx.doi.org/10.1109/ICARSC.2016.62.

[21] G. Reina, M. Foglia, On the mobility of all-terrain rovers, Ind. Robot: Int. J. 40 (2013) 5, http://dx.doi.org/10.1108/01439911311297720.

[22] G. Reina, Cross-coupled control for all-terrain rovers, Sensors 13 (1) (2013) 785–800, http://dx.doi.org/10.3390/s130100785.

[23] T. Kane, D. Levinson, Dynamics, Theory and Applications, in: McGraw-Hill series in mechanical engineering, McGraw-Hill, 1985.

[24] A.S. Rambely, N.A. Halim, R.R. Ahmad, A numerical comparison of Langrange and Kane's methods of an arm segment, Int. Mod. Phys.: Conf. Ser. 09 (2012) 68–75, http://dx.doi.org/10.1142/S2010194512005119.

[25] Z. Hussain, N.Z. Azlan, KANE's method for dynamic modeling, in: 2016 IEEE International Conference on Automatic Control and Intelligent Systems, I2CACIS, 2016, pp. 174–179, http://dx.doi.org/10.1109/I2CACIS.2016.7885310.

[26] R.S. Pal, Modelling of helicopter underslung dynamics using Kane's method, IFAC-PapersOnLine 53 (1) (2020) 536–542, http://dx.doi.org/10.1016/j.ifacol.2020.06.090, 6th Conference on Advances in Control and Optimization of Dynamical Systems ACODS 2020.

[27] R. Lindemann, Dynamic modeling and simulation of planetary rovers, in: Aerospace Design Conference, http://dx.doi.org/10.2514/6.1992-1269, URL https://arc.aiaa.org/doi/abs/10.2514/6.1992-1269, arXiv:https://arc.aiaa.org/doi/pdf/10.2514/6.1992-1269.

[28] F. Benamar, C. Grand, Quasi-static motion simulation and slip prediction of articulated planetary rovers using a kinematic approach, J. Mech. Robot. 5 (2) (2013) http://dx.doi.org/10.1115/1.4023873, 021002.

[29] F. Chen, G. Genta, Dynamic modeling of wheeled planetary rovers: A model based on the pseudo-coordiates approach, Acta Astronaut. 81 (1) (2012) 288–305, http://dx.doi.org/10.1016/j.actaastro.2012.06.008.

[30] Q. Fu, V. Krovi, Articulated wheeled robots: Exploiting reconfigurability and redundancy, in: Dynamic Systems and Control Conference, vol. ASME 2008 Dynamic Systems and Control Conference, Parts A and B, 2008, pp. 653–660, http://dx.doi.org/10.1115/DSCC2008-2193, arXiv:https://asmedigitalcollection.asme.org/DSCC/proceedings-pdf/DSCC2008/43352/653/4573914/653_1.pdf.

[31] M. Bekker, Introduction to Terrain-Vehicle Systems, University of Michigan Press, 1969.

[32] J. Wong, Theory of Ground Vehicles, Wiley, 2001.

[33] Y. chun Yang, J. song Bao, Y. Jin, Y.-I. Cheng, A virtual simulation environment for lunar rover: Framework and key technologies, Int. J. Adv. Robot. Syst. 5 (2) (2008) 16, http://dx.doi.org/10.5772/5651.

[34] K. Yoshida, H. Hamano, Motion dynamics of a rover with slip-based traction model, in: IEEE International Conference on Robotics and Automation, 2002. Proceedings, Vol. 2002, no. 3, ICRA '02, 2002, pp. 3155–3160.

[35] G. Ishigami, A. Miwa, K. Nagatani, K. Yoshida, Terramechanics-based model for steering maneuver of planetary exploration rovers on loose soil, J. Field Robot. 24 (3) (2007) 233–250, http://dx.doi.org/10.1002/rob.20187, URL https://onlinelibrary.wiley.com/doi/abs/10.1002/rob.20187.

[36] B. Schäfer, A. Gibbesch, R. Krenn, B. Rebele, Planetary rover mobility simulation on soft and uneven terrain, Veh. Syst. Dyn. 48 (1) (2010) 149–169, http://dx.doi.org/10.1080/00423110903243224.

[37] A. Gibbesch, B. Schäfer, Multibody system modelling and simulation of plenetary rover mobility on soft terrain, 2005.

[38] A. Gallina, A. Gibbesch, R. Krenn, T. Uhl, B. Schäfer, Multibody simulation of planetary rover mobility in condition of uncertain soft terrain, Procedia IUTAM 13 (2015) 118–126, http://dx.doi.org/10.1016/j.piutam.2015.01.009, Dynamical Analysis of Multibody Systems with Design Uncertainties.

[39] R. Krenn, G. Hirzinger, Simulation of rover locomotion on Sandy Terrain – modeling verification and validation, 2008.

[40] M. Sutoh, Traveling performance analysis of planetary rovers using a repeatable test system in vacuum, J. Terramech. 95 (2021) 15–24, http://dx.doi.org/10.1016/j.jterra.2021.02.003.

[41] C. Chen, M. Shu, Y. Wang, L. Ding, H. Gao, H. Liu, S. Zhou, Simultaneous control of trajectory tracking and coordinated allocation of rocker-bogie planetary rovers, Mech. Syst. Signal Process. 151 (2021) 107312, http://dx.doi.org/10.1016/j.ymssp.2020.107312.

[42] K.H. Hunt, F.R.E. Crossley, Coefficient of restitution interpreted as damping in vibroimpact, J. Appl. Mech. 42 (2) (1975) 440–445, http://dx.doi.org/10.1115/1.3423596, arXiv:https://asmedigitalcollection.asme.org/appliedmechanics/article-pdf/42/2/440/5454660/440_1.pdf.

[43] H.M. Lankarani, P.E. Nikravesh, A contact force model with hysteresis damping for impact analysis of multibody systems, J. Mech. Des. 112 (3) (1990) 369–376, http://dx.doi.org/10.1115/1.2912617, arXiv:https://asmedigitalcollection.asme.org/mechanicaldesign/article-pdf/112/3/369/5520668/369_1.pdf.

[44] L. Skrinjar, J. Slavič, M. Boltežar, A review of continuous contact-force models in multibody dynamics, Int. J. Mech. Sci. 145 (2018) 171–187, http://dx.doi.org/10.1016/j.ijmecsci.2018.07.010.

[45] C. Makkar, W.E. Dixon, W.G. Sawyer, G. Hu, A new continuously differentiable friction model for control systems design, in: Proceedings, 2005 IEEE/ASME International Conference on Advanced Intelligent Mechatronics, 2005, pp. 600–605, http://dx.doi.org/10.1109/AIM.2005.1511048.